Convergent-Beam EMCD: Benefits, Pitfalls, and Applications

S. Löffler[a,b,*], W. Hetaba[a,1]

[a]*University Service Centre for Transmission Electron Microscopy, TU Wien, Vienna, Austria*
[b]*Dept. for Materials Science and Engineering, McMaster University, Hamilton, Ontario, Canada*

Abstract

Energy-loss magnetic chiral dichroism (EMCD) is a versatile method for studying magnetic properties on the nanoscale. However, the classical EMCD technique is notorious for its low signal to noise ratio (SNR), which is why many experimentalists have adopted a convergent beam approach. Here, we study the theoretical possibilities of using a convergent beam for EMCD. In particular, we study the influence of detector positioning as well as convergence and collection angles on the detectable EMCD signal. In addition, we analyze the expected SNR and give some guidelines for achieving optimal EMCD results.

Keywords: EMCD, convergence angle, collection angle, aperture position, signal-to-noise ratio, STEM

*Corresponding author
 Email address:* `stefan.loeffler@tuwien.ac.at` (S. Löffler)
[1]Currently at Fritz-Haber-Institut der Max-Planck-Gesellschaft, Berlin, Germany

1. Introduction

Electron magnetic chiral dichroism (EMCD), the electron microscopic equivalent to X-ray magnetic circular dichroism (XMCD), is a very versatile tool for investigating magnetic materials on the nanometer scale. Ever since its theoretical prediction [1] and subsequent realization [2], EMCD has been gaining popularity in many fields, including magnetic nano-engineering and spintronics.

There are, however, two severe limitations with the classical EMCD approach: spatial resolution and signal-to-noise (SNR) ratio. In the classical EMCD approach, one sends a plane wave into a crystal that was tilted into systematic row condition and subsequently measures the inelastically scattered electrons at particular points of the diffraction plane far away from the diffraction spots (see also fig. 1). While plane waves are well-suited for an elegant theoretical treatment, they are not so useful in practice. First of all, from a fundamental point of view, it is impossible to actually create or measure true plane waves, due to the limited extent of the microscope and the apertures, as well as the beam rotation induced by the magnetic lenses [3]. Secondly, from an experimental point of view, a (quasi) plane wave has a very low current density at the sample. Together with the fact that the signal has to be measured off-axis — where it can be orders of magnitude smaller than on-axis — with (ideally infinitely) small detectors, this results in a notoriously low SNR. Another issue is resolution. When acquiring spectra in diffraction mode, the spatial resolution is usually defined by using a selected area aperture (typically of the order of 100 nm), thereby reducing the signal even further. Alternatively, one can measure in image mode using energy-filtered TEM (EFTEM) [4, 5]. Due to the required energy-slit, this again leads to low intensity, in addition to poor energy resolution.

To overcome these limitations, several new approaches have been proposed and tested, ranging from alternative measurement geometries in scanning transmission electron microscopy (STEM) [6–10], over vortex beams [11–13], to the use of aberration correctors to manipulate the phase of the electron beam [14, 15]. However, all these methods exhibit very low signal, are typically limited to atomic resolution [16, 17], and may require changing components of the microscope or operating it under non-standard conditions. Thus, these new methods are not yet applicable for many practical applications.

However, there is a third alternative that has gained increasing popularity in experimental EMCD in recent years: convergent-beam EMCD. It improves both the spatial
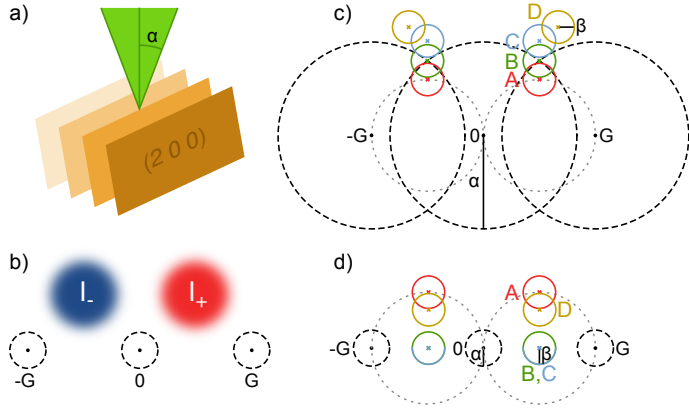
Figure 1: Sketch of the convergent beam setup. (a) The incident beam with convergence semi-angle α is centered on a crystal plane. (b) Sketch of the general positions of the areas with "positive" (i.e., higher than non-magnetic) signal I_+ and "negative" (i.e., lower than non-magnetic) signal I_-. (c) Schematic elastic diffraction pattern for large α. (d) Schematic elastic diffraction pattern for small α. The diffraction spots are labeled 0, G, -G. Diffraction disks are depicted as black dashed lines, the Thales circles are depicted as gray dotted lines. α is the convergence semi-angle, β is the collection semi-angle. The four detector positions A–D are described in the text.

resolution and the SNR at the same time while still making use of the original, straightforward measurement setup by using a convergent beam and finite collection apertures instead of plane waves. This method has been used experimentally to boost the spatial resolution of classical EMCD (see, e.g., [18–24], and it has long been known that large collection apertures can improve the SNR [25]. Therefore, it is surprising that, to our knowledge, the influence of the convergence angle and the effect the interplay between convergence and collection angle has on both the signal and the SNR has not been studied extensively from a theoretical point of view so far (although it has been studied, e.g., for aberrated probes [26]).

In this work, we present simulations that show that convergent beam EMCD is in many ways superior to classical EMCD. In particular, we present simple rules of thumb for how to obtain close-to-optimal SNR while at the same time improving the spatial resolution to close to atomic resolution. This is expected to open new avenues for optimizing EMCD measurements in general, but particularly for the characterization of fine grained materials, thin films, as well as the magnetic structure in the vicinity of interfaces and defects. Thus, it is expected to lead to great advances in material science.

2. Methods

In this work, we present extensive simulations for the model system of a 10 nm thick bcc Fe crystal, tilted 10° from the [0 0 1] zone axis (ZA) to produce a systematic row case

including the $(2\,0\,0)$ diffraction spot. All simulations were performed using an acceleration voltage of $300\,\text{kV}$ without spherical aberration[2]. The beam was focused (with varying convergence semi-angle α) onto the entry surface of the sample and positioned on an atomic plane. The complete measurement setup is depicted in fig. 1.

The inelastic scattering was performed using the mixed dynamic form factor (MDFF) approach [2, 27, 28]. The MDFF was modeled with an idealized fully spin-polarized cross-density of states [28] and Slater-type orbital wavefunctions [29], taking into account the dipole allowed transitions $2p \to d$. The elastic scattering both before and after the inelastic scattering were taken into account using the multislice algorithm [30]. A 2048×2048 grid with ca. $0.09\,\text{Å/px}$ was used together with a slice thickness of $1\,\text{Å}$ and the electrostatic potentials given by Kirkland [30].

For extracting the EMCD effect, one needs to measure and compare the signal strengths at two different positions I_+, I_-. In the context of this work, two different (albeit closely related) definitions of the EMCD effect are used. On the one hand, we use the "difference signal", sometimes also refered to as "absolute EMCD effect", defined as

$$I_0 = \frac{I_+ + I_-}{2}. \tag{1}$$

On the other hand, we use the "quotient signal", sometimes also refered to as "relative signal", defined as

$$S = 2 \cdot \frac{I_+ - I_-}{I_+ + I_-} = \frac{\Delta I}{I_0}. \tag{2}$$

The quotient signal is the one originally proposed (up to the prefactor of 2) and used in several later works [1, 5, 7, 31–33]. By dividing by the average intensity I_0, it is automatically normalized to the incident dose — although it still depends on the sample thickness. For quantitative work, the difference signal is method of choice as it allows the application of sum rules for determining the m_l/m_s ratio [34–36].

To find the optimal conditions for extracting an EMCD signal, two different schemes were used. On the one hand, a pointwise comparison of corresponding points on the upper/lower or left/right halves of the diffraction plane was performed to obtain a visual indication of the distribution of the EMCD effect. On the other hand, circular collection apertures (of varying collection semi-angle β) were centered at four different sets of

---

[2]The spherical aberration is not expected to play a major role here, though, as we are working mostly in the diffraction plane.

points of the diffraction plane: (A) on the Thales circle, (B) at the intersection of adjacent elastic diffraction disks[3], (C) just outside the elastic diffraction disks such that the collection aperture touched adjacent diffraction disks[4], (D) in an "optimal position", i.e. at a convergence and collection angle dependent point determined by a downhill simplex optimization algorithm [37] where the maximal EMCD effect can be obtained. All four positions are also depicted schematically in fig. 1.

3. Results

3.1. Position of the EMCD Effect

In order to check the applicability of convergent beam EMCD, it is first necessary to determine where an EMCD effect can be expected in the diffraction plane (if at all). To that end, fig. 2a–d show simulated energy filtered diffraction patterns for the Fe L_3 edge for different convergence angles. For classical EMCD (i.e., the first column in fig. 2), it is well known that there are four areas exhibiting magnetic information, one in each quadrant of the diffraction plane. Therefore, in fig. 2e–h, we plotted the difference EMCD effect ΔI calculated pixel by pixel from the difference of the upper and the lower half-plane. Likewise, fig. 2i–l, show the difference EMCD effect ΔI calculated pixel by pixel from the difference of the right and the left half-plane. Fig. 2m–p show the quotient EMCD effect S calculated from the difference of the upper and lower half-plane, while fig. 2q–t show the quotient EMCD effect S calculated from the difference of the right and left half-plane.

The first main result from those maps is that with increasing convergence angle, the areas where the quotient EMCD is strong is "pushed out" such that it can generally be found close to the rim of the elastic diffraction disks. The same is mostly true also for the left/right half-plane subtracted difference signal (fig. 2i–l). Only the top/bottom subtracted difference signal (fig. 2e–h) exhibits strong signal inside the diffraction disks which can be attributed to artifacts caused by the Ewald sphere curvature as discussed below.

The fact that the areas with strong EMCD signal are "pushed out" can be explained qualitatively by considering the relative contributions of the different scattering vectors.

---

[3]In case the elastic diffraction disks did not overlap, the apertures were centered on the systematic row

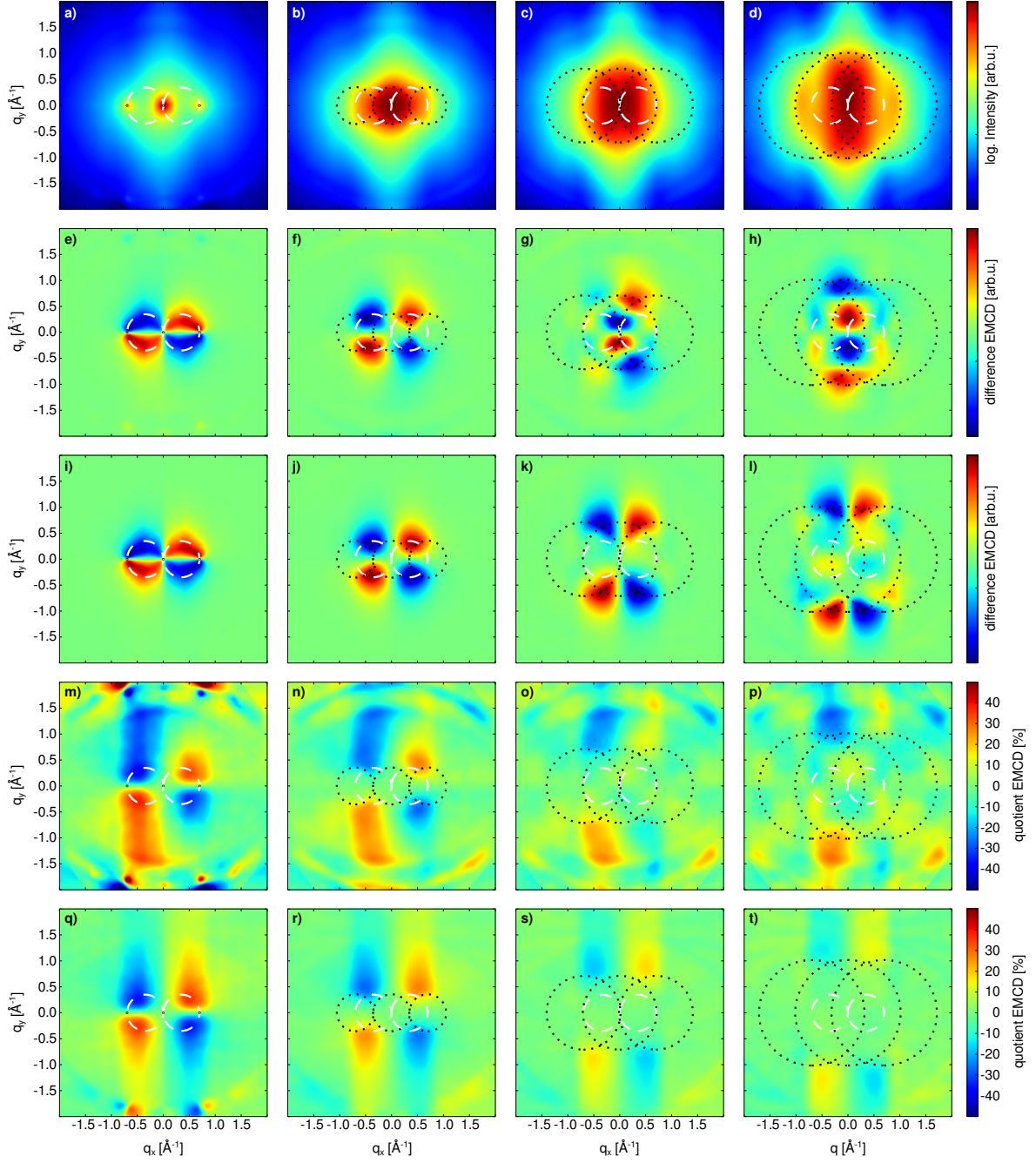[4]In case such a touching configuration was not possible, the aperture was positioned on the systematic row

Figure 2: Energy-filtered diffraction patterns (a–d), pointwise difference EMCD maps based on upper/lower halfplane subtraction (e–h), pointwise difference EMCD maps based on left/right halfplane subtraction (i–l), pointwise quotient EMCD maps based on upper/lower halfplane subtraction (m–p) and pointwise quotient EMCD maps based on left/right halfplane subtraction (q–t) for convergence semi-angles of 0 mrad (a, e, i, m, q), 7 mrad (b, f, j, n, r), 14 mrad (c, g, k, o, s), and 20 mrad (d, h, l, p, t). The black dotted circles indicate the three most intense diffraction disks, whereas the white dashed circles indicate the classical Thales circles. The energy-filtered diffraction patterns are shown in contrast-optimized logarithmic scale.

Assuming ideal conditions, a point-like detector, and using the dipole approximation [7, 38, 39], the EMCD difference signal is proportional to

$$\int \frac{\vec{q} \times \vec{q'}}{q^2 q'^2} d^2q \, d^2q', \tag{3}$$

where one has to integrate over *all* combinations of scattering vectors connecting points inside the convergence disks (with radii α, see Fig. 1) with the point-like detector. Due to the $1/(q^2 q'^2)$ dependence, contributions from short scattering vectors are dominant and due to the $\vec{q} \times \vec{q'}$ dependence, contributions are strongest for perpendicular scattering vectors.

In the limit of small convergence angles, only one pair of scattering vectors is possible and the situation reduces to the case of classical EMCD: the perpendicularity requirement suggests that the signal is strongest close to the Thales circle.[5] For large convergence angles, this explanation no longer holds as then, many combinations of scattering vectors can contribute.

First, we consider detector positions inside the diffraction disks. Without loss of generality, we will assume a detector position inside the 0 diffraction disk. As stated above, the dominant contributions stem from short scattering vectors. For the sake of simplicity, we assume that the complex prefactor coming from elastic scattering is approximately constant in the immediate surrounding of the detector where $|\vec{q}|$ is small. For any sufficiently short scattering vector $\vec{q}$ from a point inside the diffraction disk to the detector, the scattering vector $-\vec{q}$ also connects a point inside the diffraction disk to the detector. As the contributions of $(\vec{q}, \vec{q'})$ and $(-\vec{q}, \vec{q'})$ are equal in magnitude but opposite in sign for any scattering vector $\vec{q'}$, all these contributions will average out. This implies that inside the elastic diffraction disks, the difference EMCD effect will be small. In addition, the very strong total intensity inside the diffraction disks will cause the quotient EMCD effect to be suppressed even stronger than the difference EMCD effect.

Secondly, if the detector is positioned far away from large diffraction disks, neither the perpendicularity constraint nor the shortness requirement can be fulfilled, thus leading to an asymptotically vanishing EMCD effect.

Thirdly, if the detector is positioned close to the intersection of the diffraction disks,

---

[5]The exact position depends on the characteristic momentum transfer $q_z = q'_z$, as well as the details of the elastic scattering.

there are always pairs of scattering vectors that are short and fulfill the orthogonality requirement, thus yielding an appreciable EMCD effect.

From fig. 2, it is also obvious that the upper/lower difference shows severe left/right differences, particularly for larger scattering angles. The origin of these different symmetry properties can be found in the tilting of the Ewald sphere with respect to the crystal and the influence of higher order Laue zones (HOLZs), causing an inherent upper/lower asymmetry of the signal [40–42]. Some artifacts introduced by the HOLZ can be seen particularly well close to the edges of fig. 2m[6]. Due to the asymmetric Ewald sphere and the HOLZ contributions, the intensity in the upper half-plane is slightly lower than the corresponding intensity in the lower half-plane. While this intensity difference is not caused by the spin-polarization of the sample, it can easily be misinterpreted as a "fake" EMCD effect. While this is of some concern already for classical EMCD, where one typically measures at the Thales circle, it does become a vital issue for larger convergence angles, where one is forced to measure at larger scattering angles. Especially when dealing with the difference EMCD signal, the upper/lower asymmetry can give rise to very large artifacts (see fig. 2g,h). One way to overcome this could be to use the double-difference technique [35].

However, as the setup is symmetric with respect to a right/left mirror operation[7], the right/left difference maps do not suffer from this effect. Therefore, in the remainder of this work, we use the right/left difference method to extract EMCD signals.

3.2. EMCD Signal Strength and SNR

In this section, we will analyze both the achievable signal strengths ΔI and S as well as the SNR $\Delta I/\delta \Delta I$ and $S/\delta S$ associated with them as a function of convergence and collection angles for the four detector positions A–D defined above. This is conceptionally similar to previous studies that included estimations for the SNR for plane wave illumination [25] and for aberrated probes [26]. To calculate the SNR, we will include the pre-edge background intensity B which does not contribute to the signal but does increase the noise. We will also use the jump ratio defined by

$$r = \frac{I_0 + B}{B} \tag{4}$$

---

[6]Note that the figures show only a subset of the total simulated area, so the "artifacts" close to the edge are not calculation artifacts but actually coincide with HOLZ reflections consistent for the chosen scattering geometry.

[7]Provided the sample is oriented in a perfect systematic row condition [4, 42].
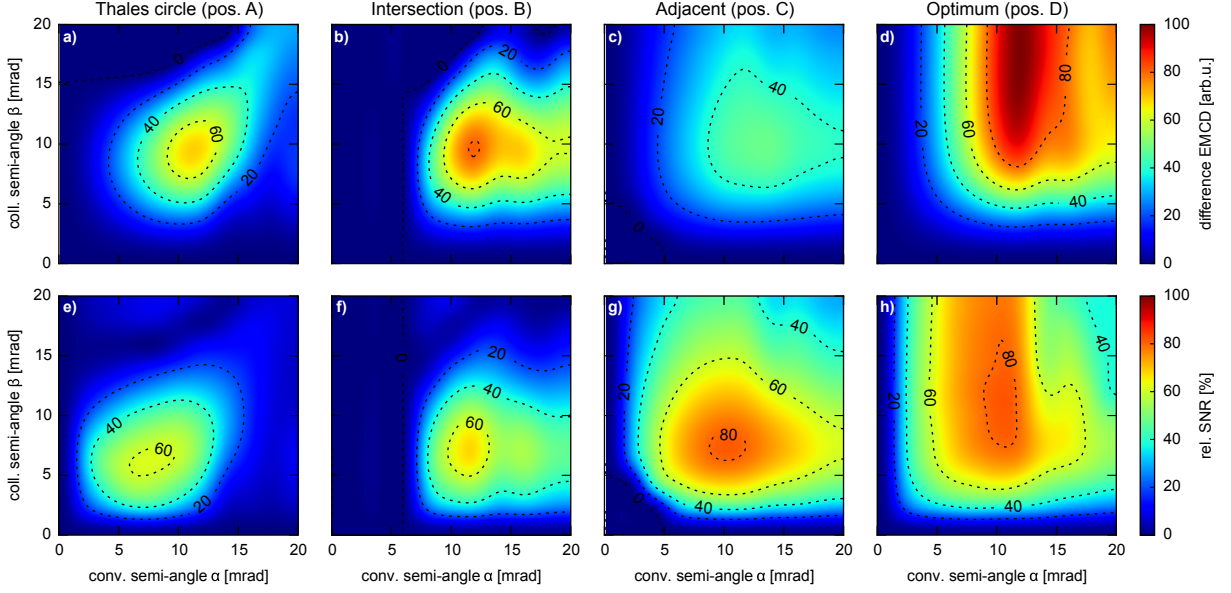
Figure 3: Difference signal ΔI (a–d) and SNR $\Delta I/\delta\Delta I$ (e–h) for the four sets of detector positions A–D as a function of convergence and collection semi-angles. The SNR is given for a jump ratio of $r = 2$ in fractions of the maximum SNR.

to simplify the equations.

Note that while we will give general formulas that should be applicable to all cases at the beginning of each section, further derivations will be based on the assumption of pure Poissonian shot noise to derive simplified formulas and actual numbers. This neglects other noise sources such as read-out noise and electronic noise (which will be low compared to the shot noise for the intensity requirements derived below), or uncertainties introduced by the background subtraction process [43]. Nevertheless, the numbers calculated below will give a good rule of thumb for the intensity necessary to obtain a statistically significant EMCD signal.

In addition, the EMCD signal strength itself will depend on a number of parameters, including the sample material, sample thickness, and scattering geometry. Therefore, angles will be discussed in relation to the Bragg angle (here: $\theta_B \approx 6.9$ mrad) and may differ in different systems.

3.2.1. Difference EMCD Effect

First, we will treat the difference EMCD effect ΔI which is most useful for quantifying EMCD signals using sum rules [34]. Fig. 3a–d shows the difference EMCD signal dependence on the convergence and collection semi-angles for the four sets of detector positions A–D defined above. The first thing that catches the eye is the fact that if the convergence or the collection angle (or both) are small, both the difference EMCD signal and the SNR

vanish. This is to be expected as in those cases the overall intensity decreases rapidly, which is why experimentalists started using convergent beam EMCD in the first place. However, using extremely large collection angles is usually not recommended either, as then positive and negative contributions to the difference EMCD signal could average out.

From fig. 3, it is apparent that positioning the detectors on the Thales circle (position A) gives a large signal (albeit not the best SNR) when both the convergence and collection angle are slightly larger than the Bragg angle. This is due to the "pushing out" of the area of strong difference EMCD signal with increasing convergence angle (see also fig. 2), combined with the increasing intensity for larger convergence angles. Compared to the Thales circle position, the intersection position (position B) gives both better overall signal and better SNR. In fact, one can reach 80 % of the optimal signal at about 70 % of the optimal SNR in the present case. The adjacent position (position C) yields a lower signal overall, but a nearly optimal SNR. In addition, it allows to use a relatively large range of convergence and collection angles with little to no impact on signal strength and SNR. Finally, the optimum position (position D) data is shown for reference.

To calculate the SNR, the following approach was used. If shot noise dominates over other noise sources (such as read out noise), $I_{\pm}$ follows a Poisson distribution. By the central limit theorem, this can be approximated well by a Gaussian distribution with a standard deviation of $\delta I_{\pm} = \sqrt{I_{\pm} + B}$ for sufficiently large signal, where B is the background intensity. Then the variance $(\delta \Delta I)^2$ of the signal ΔI is given by

$$(\delta \Delta I)^2 = (\delta I_+)^2 + (\delta I_-)^2 = I_+ + I_- + 2B = 2(I_0 + B). \tag{5}$$

Therefore, the SNR reads

$$\frac{\Delta I}{\delta \Delta I} = \frac{I_+ - I_-}{\sqrt{(\delta I_+)^2 + (\delta I_-)^2}} = \frac{S I_0}{\sqrt{2(I_0 + B)}} \tag{6}$$

Not surprisingly, the SNR increases with total intensity I_0 and dichroic fraction (quotient signal) S while it decreases with pre-edge background B. A similar expression was also reported for maps with an aberrated probe [26], although for larger convergence angles.

To answer the question of how many counts need to be recorded to achieve a certain statistical significance, one naturally needs to consider the ratio between the elemental edge and the pre-edge background (which increases the noise level but not the signal). Assuming a jump ratio r of

$$r = \frac{I_0 + B}{B} \quad \Leftrightarrow \quad B = \frac{I_0}{r - 1} \quad \Leftrightarrow \quad I_0 + B = I_0 \cdot \frac{r}{r - 1}, \tag{7}$$
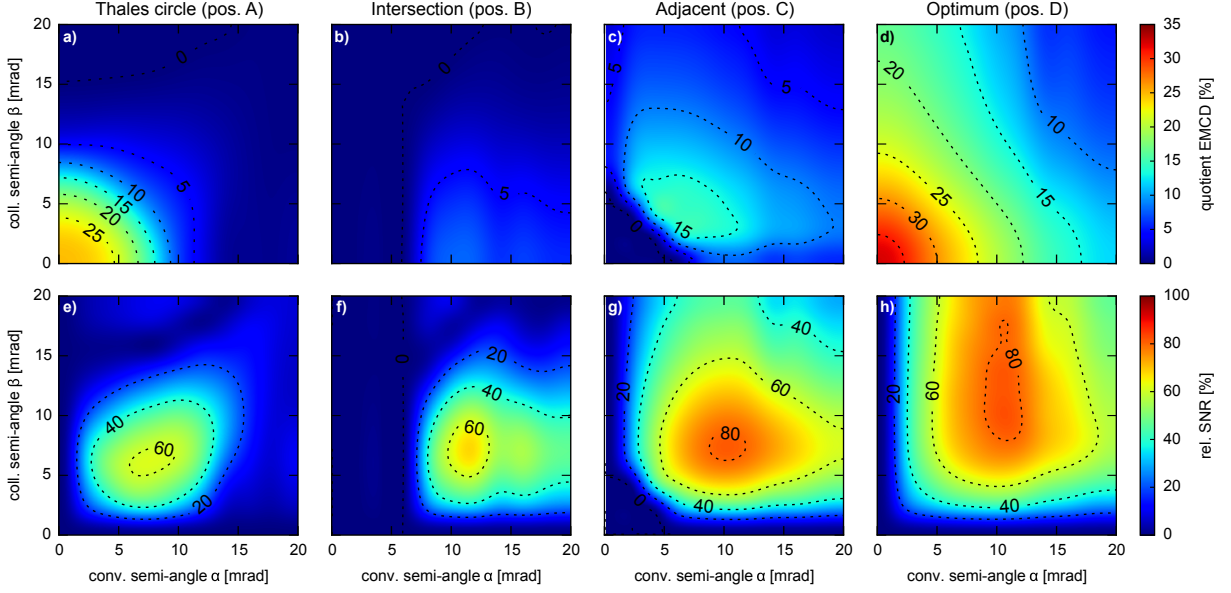
10

Figure 4: EMCD effect S (a–d) and SNR $S/\delta S$ (e–h) for the four sets of detector positions A–D as a function of convergence and collection semi-angles. The SNR is given for a jump ratio of $r = 2$ in fractions of the maximum SNR.

the SNR can be rewritten as

$$\frac{\Delta I}{\delta \Delta I} = \frac{S\sqrt{I_0(r-1)}}{\sqrt{2r}}. \tag{8}$$

If $B = I_0$, i.e. for a jump ratio of $r = 2$, the SNR takes the form

$$\frac{\Delta I}{\delta \Delta I} = \frac{\Delta I}{2\sqrt{I_0}} = \frac{S\sqrt{I_0}}{2}. \tag{9}$$

To reach an SNR of k, one needs to achieve a total intensity of

$$I_0 + B \geq \frac{2r^2 k^2}{S^2(r-1)^2} \tag{10}$$

counts. This prediction is in good agreement with the order of magnitude of the intensity threshold found experimentally [24]. For the special case of $k = 3$ and $r = 2$, this gives

$$I_0 + B \geq \frac{72}{S^2} \tag{11}$$

i.e., for an expected dichroic fraction of $S = 10\,\%$, an intensity of at least 7200 counts needs to be achieved in this case.

3.2.2. Quotient EMCD Effect

Fig. 4a–d show the dependence of the quotient EMCD effect on the convergence and collection angles for the four different sets of detector positions A–D defined above. As was already noted in sec. 3.1, placing the detectors on the Thales circle (position A) only gives a large EMCD signal for small convergence and collection angles. For angles larger

11

than roughly θ_B, the signal decreases rapidly as one is then measuring "inside" the elastic diffraction disk, which will increase I_0 and therefore decrease S. Putting the detectors on the intersection of the elastic diffraction disks (position B) gives an extremely low quotient signal, unlike the difference signal. Again, this is due to the fact that there is a strong contribution to I_0 inside the diffraction disks which will strongly decrease the quotient signal. Putting the detectors adjacent to the elastic diffraction disks (position C) gives a medium quotient EMCD effect, but over a large range of convergence and collection angles, similar to the difference EMCD signal. Also like the difference signal, the SNR is close to optimal in this case. In addition, it is interesting to note that the adjacent position is mostly complementary to the Thales circle position in terms of quotient signal. Finally, the optimum position (position D) is shown for reference.

For calculating the SNR, the same assumption as for the difference signal case are used. Here, the variance $(\delta S)^2$ of the signal S can be calculated by error propagation to read

$$(\delta S)^2 = 16 \cdot \frac{(\delta I_+)^2 I_-^2 + I_+^2 (\delta I_-)^2}{(I_+ + I_-)^4}. \tag{12}$$

with a SNR of

$$\frac{S}{\delta S} = \frac{I_+^2 - I_-^2}{2\sqrt{(\delta I_+)^2 I_-^2 + I_+^2 (\delta I_-)^2}}. \tag{13}$$

The former can be simplified to

$$(\delta S)^2 = \frac{16 I_+ I_-}{(I_+ + I_-)^3} + 16 B \cdot \frac{I_+^2 + I_-^2}{(I_+ + I_-)^4} \tag{14}$$

By virtue of

$$I_+ - I_- = S I_0$$
$$I_+ + I_- = 2 I_0$$
$$4 I_+ I_- = I_0^2 (4 - S^2)$$
$$2(I_+^2 + I_-^2) = I_0^2 (4 + S^2)$$
$$\tag{15}$$

this can also be written as

$$(\delta S)^2 = \frac{I_0(4 - S^2) + B \cdot (4 + S^2)}{2 I_0^2}. \tag{16}$$

Thus, the SNR becomes

$$\frac{S}{\delta S} = \frac{\sqrt{2} S I_0}{\sqrt{I_0(4 - S^2) + B \cdot (4 + S^2)}}. \tag{17}$$

This can also be written in terms of the jump ratio as

$$\frac{S}{\delta S} = \frac{\sqrt{2I_0}S}{\sqrt{4 - S^2 + \frac{4 + S^2}{r-1}}} = \frac{S\sqrt{2(r-1)I_0}}{\sqrt{r(4 - S^2) + 2S^2}}.$$ (18)

If $B = I_0$, i.e. for a jump ratio of $r = 2$, the SNR takes the same form as for the difference EMCD signal, i.e.,

$$\frac{S}{\delta S} = \frac{S\sqrt{I_0}}{2}.$$ (19)

To reach a SNR of at least k, I_0 must be chosen such that

$$I_0 \geq \frac{k^2}{2S^2}\left(4 - S^2 + \frac{4 + S^2}{r - 1}\right)$$ (20)

or, equivalently, that the total intensity fulfills

$$I_0 + B \geq \frac{k^2 r}{2S^2(r - 1)}\left(4 - S^2 + \frac{4 + S^2}{r - 1}\right)$$ (21)

For the special case of $k = 3$ and $r = 2$, this again gives

$$I_0 + B \geq \frac{72}{S^2}.$$ (22)

4. Discussion

4.1. Difference EMCD Effect vs. Quotient EMCD Effect

As mentioned above, the difference EMCD signal is the one typically used for quantification due to the applicability of sum rules. However, in some cases determining the m_l/m_s ratio may not be required. Instead, it might be sufficient to check if there is any dichroic signal at all or how it changes, e.g. with position across defects. In such cases, using the quotient signal instead of the difference signal may even be beneficial in terms of SNR, as a comparison of eq. 17 and eq. 6 shows:

$$\frac{\sqrt{2}SI_0}{\sqrt{I_0(4 - S^2) + B \cdot (4 + S^2)}} < \frac{SI_0}{\sqrt{2(I_0 + B)}}$$ (23)

$$4(I_0 + B) < I_0(4 - S^2) + B \cdot (4 + S^2)$$ (24)

$$0 < S^2 \cdot (B - I_0)$$ (25)

This means that only for $B > I_0 \Leftrightarrow r < 2$, i.e. for thick specimens, using the difference signal is actually better than using the quotient signal in terms of SNR. However, thick specimens typically yield a low overall EMCD effect owing to oscillations and sign reversal caused by the elastic scattering and pendellösung [32, 39]. Therefore, the quotient signal should be prefered unless the application of sum rules is required.
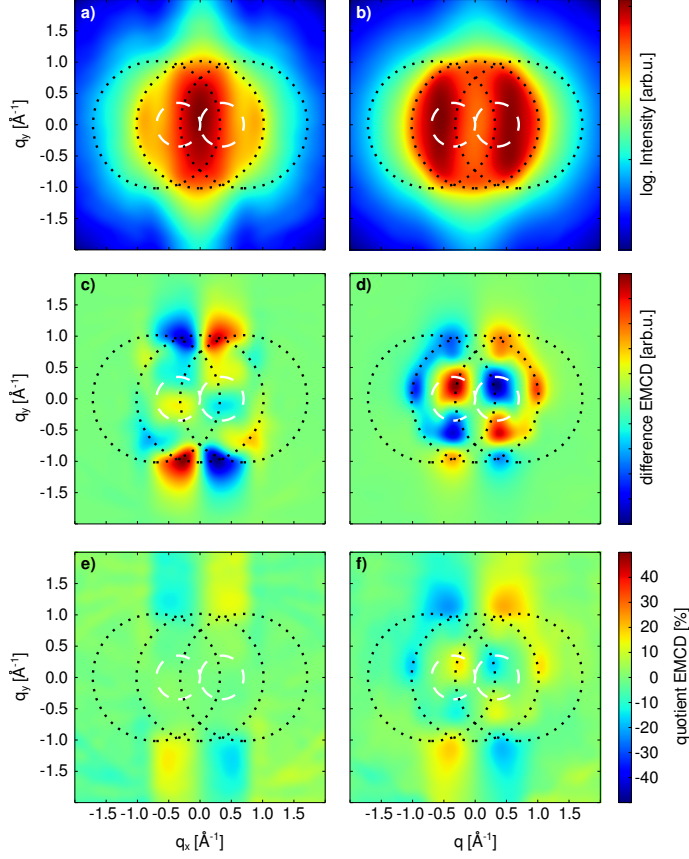
Figure 5: Energy-filtered diffraction patterns (a, b), pointwise difference EMCD maps based on left/right halfplane subtraction (c, d) and pointwise quotient EMCD maps (e, f) for on-plane (a, c, e) and off-plane (b, d, f) beam positions. The convergence semi-angle is 20 mrad. The black dotted circles indicate the three most intense diffraction disks, whereas the white dashed circles indicate the classical Thales circles. The energy-filtered diffraction patterns are shown in contrast-optimized logarithmic scale.

4.2. Beam Position Dependence

In this section, we investigate the dependence of the convergent beam EMCD signal on the beam position. For small convergence and collection angles, one can expect that the EMCD signal is largely independent of the beam position due to the large illuminated area and, consequently, the low spatial resolution. For convergence and collection semi-angles significantly larger than the Bragg angle, however, one can expect a position-dependence [10]. To study the effect this has on the signal strengths at the various detector positions as well as on the SNR, we also performed calculations with the beam displaced by half a lattice plane distance so that it was positioned directly in-between adjacent lattice planes.

Fig. 5 compares the energy-filtered diffraction patterns and point-wise EMCD effects for on-plane and off-plane beam positions for a large convergence angle. While there are obvious differences, it is remarkable that both difference and quotient EMCD effects with the same sign can be found at similar positions adjacent to the diffraction disks.
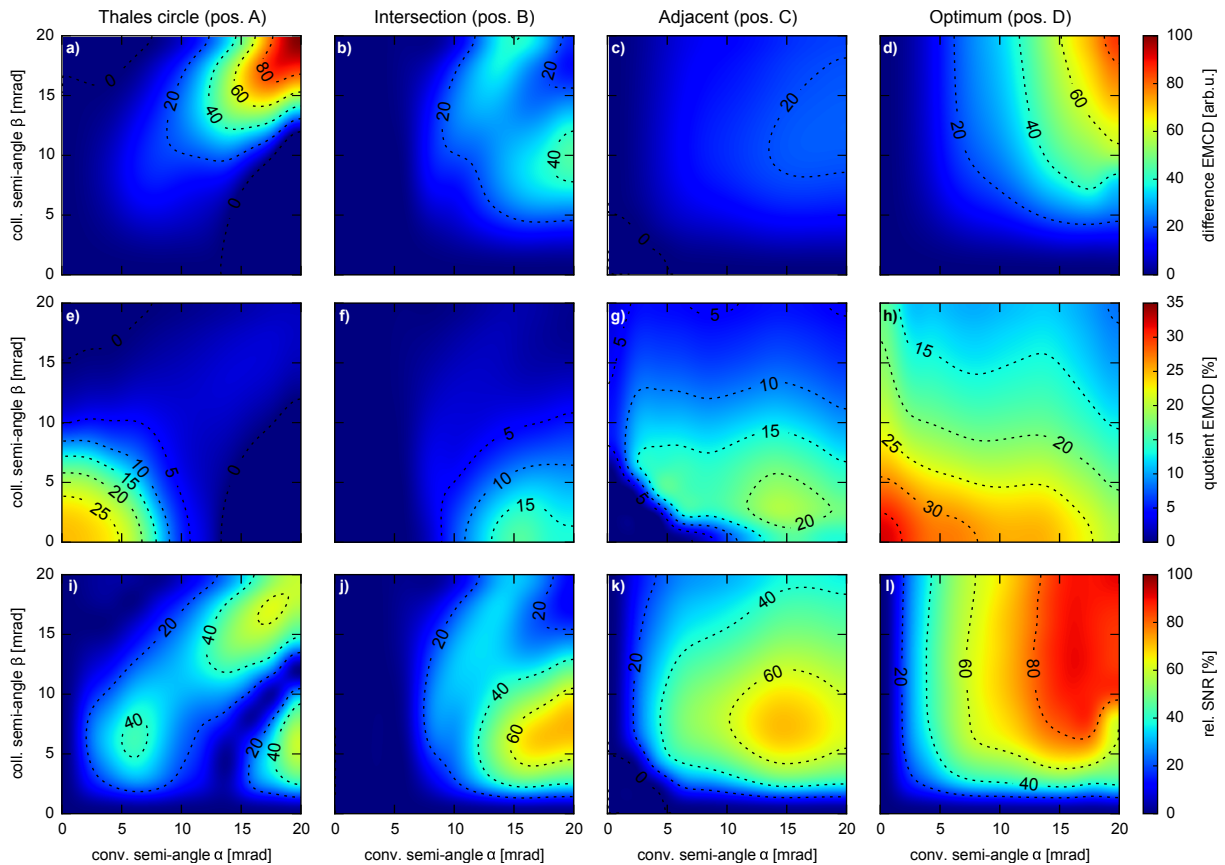
14

Figure 6: Difference EMCD effect (a–d), quotient EMCD effect (e–h) and SNR (i–l) for the four sets of detector positions A–D as a function of convergence and collection semi-angles for a beam position in-between atomic planes. The SNR is given for a jump ratio of $r = 2$ in fractions of the maximum SNR.

While these contributions from adjacent positions are weaker for the difference signal (with stronger contibutions with reversed sign showing up close to the Thales circle), the quotient EMCD effect is even stronger for the off-plane condition than for the on-plane condition. Qualitatively, this can be understood from the fact that the inelastic scattering kernels contributing to EMCD have the same shape as electron vortex beams: an azimuthal phase ramp combined with a donut-shaped intensity distribution [28, 44, 45]. Thus, the highest probability for exciting a transition that contributes to the EMCD signal with a very small probe is actually not on the atomic nuclei, but in the area surrounding them.[8] Of course, the question of how much which atom contributes to the EMCD effect depends crucially on how the incident and outgoing electron beams channel through the crystal [46, 47]. However, a full quantitative description of the resulting thickness dependence is beyond the scope of this work.

---

[8]This can also be understood from the fact that the initial p-states contributing to the L-edge have vanishing probability density at the position of the nucleus.

Fig. 6 shows the convergence and collection semi-angle dependence of the EMCD signals for a probe beam positioned between atomic planes, together with the corresponding SNR (which, for the chosen jump ratio of $r = 2$, is the same for the difference and for the quotient signal). Qualitatively, it looks similar to the on-plane case depicted in fig. 4. In particular for small convergence and collection semi-angles, the maps are identical, as is to be expected. However, at larger angles, several changes are visible. Note that this is actually wanted in order to be able to perform lattice-resolved EMCD experiments [10].

Perhaps the most striking difference is the large difference signal enhancement at the Thales circle for large convergence and collection angles. This is in agreement with fig. 5 which shows the well-known strong position-dependence of the intensity in the regions of overlapping diffraction disks, leading to the appearance of a strong EMCD difference signal close to the Thales circle. In addition, for the intersection and adjacent positions, the difference signal is somewhat decreased. Interestingly, the quotient signal shows an increase at the same positions. Regarding the SNR, the same general trend is seen at the off-plane beam position as at the on-plane beam position: the highest values can usually be achieved at medium angles, in this case particularly with convergence angles of approximately $2\theta_B$ (i.e. slightly larger than on-plane) and collection angles of ca. θ_B (i.e. slightly smaller than on-plane).

5. Concluding Remarks

In this work, we have explored the possibilities of convergent-beam EMCD using numerical simulations. We found that this method gives similar EMCD signals as the classical, parallel beam EMCD method while having superior SNR characteristics, in accordance with previous works. As a rule of thumb, choosing a convergence semi-angle slightly larger than the Bragg angle, a collection angle close to the Bragg angle, and positioning the collection aperture just outside the elastic diffraction disks should give close to optimal results. In addition, we estimated that more than approximately 7200 counts at the edge under investigation are required (the exact value will depend on the peak-to-background ratio and the expected dichroic fraction, which, in turn, will depend on the sample material, thickness, and orientation as well as the scattering geometry).

Especially the improvements in SNR, as well as in spatial resolution, open exciting new possibilities for EMCD that may soon lead to an even broader applicability of this exciting technique for material science.

Bibliography

[1] C. Hébert, P. Schattschneider, A proposal for dichroic experiments in the electron microscope, Ultramicroscopy 96 (3-4) (2003) 463 – 468. `doi:10.1016/S0304-3991(03)00108-6`.

[2] P. Schattschneider, S. Rubino, C. Hebert, J. Rusz, J. Kunes, P. Novák, E. Carlino, M. Fabrizioli, G. Panaccione, G. Rossi, Detection of magnetic circular dichroism using a transmission electron microscope, Nat. 441 (2006) 486–488. `doi:10.1038/nature04778`.

[3] D. Eyidi, C. Hébert, P. Schattschneider, Short note on parallel illumination in the tem, Ultramicroscopy 106 (11-12) (2006) 1144 – 1149. `doi:10.1016/j.ultramic.2006.04.029`.

[4] H. Lidbaum, J. Rusz, S. Rubino, A. Liebig, B. Hjörvarsson, P. M. Oppeneer, O. Eriksson, K. Leifer, Reciprocal and real space maps for emcd experiments, Ultramicroscopy 110 (11) (2010) 1380 – 1389. `doi:10.1016/j.ultramic.2010.07.004`.

[5] M. Stöger-Pollach, C. Treiber, G. Resch, D. Keays, I. Ennen, Emcd real space maps of magnetospirillum magnetotacticum, Micron 42 (5) (2011) 456 – 460. `doi:10.1016/j.micron.2011.01.003`.

[6] P. Schattschneider, I. Ennen, M. Stöger-Pollach, J. Verbeeck, V. Mauchamp, M. Jaouen, Real space maps of magnetic moments on the atomic scale: Theory and feasibility, Ultramicroscopy 110 (8) (2010) 1038 – 1041. `doi:10.1016/j.ultramic.2009.11.020`.

[7] P. Schattschneider, I. Ennen, S. Löffler, M. Stöger-Pollach, J. Verbeeck, Circular dichroism in the electron microscope: Progress and applications (invited), J. Appl.

Phys. 107 (9) (2010) 09D311. `doi:10.1063/1.3365517`.
URL `http://link.aip.org/link/?JAP/107/09D311/1`

[8] P. Schattschneider, J. Verbeeck, V. Mauchamp, M. Jaouen, A.-L. Hamon, Real-space simulations of spin-polarized electronic transitions in iron, Phys. Rev. B 82 (2010) 144418. `doi:10.1103/PhysRevB.82.144418`.

[9] P. Schattschneider, B. Schaffer, I. Ennen, J. Verbeeck, Mapping spin-polarized transitions with atomic resolution, Phys. Rev. B 85 (2012) 134422. `doi:10.1103/PhysRevB.85.134422`.

[10] J. Rusz, S. Muto, J. Spiegelberg, R. Adam, K. Tatsumi, D. E. Bürgler, P. M. Oppeneer, C. M. Schneider, Magnetic measurements with atomic-plane resolution, Nature communications 7 (2016) 12672. `doi:10.1038/ncomms12672`.

[11] J. Verbeeck, H. Tian, P. Schattschneider, Production and application of electron vortex beams, Nat. 467 (7313) (2010) 301–304. `doi:10.1038/nature09366`.

[12] D. Pohl, S. Schneider, J. Rusz, B. Rellinghaus, Electron vortex beams prepared by a spiral aperture with the goal to measure EMCD on ferromagnetic films via STEM, Ultramicroscopy 150 (2015) 16 – 22. `doi:http://dx.doi.org/10.1016/j.ultramic.2014.11.025`.
URL `http://www.sciencedirect.com/science/article/pii/S0304399114002411`

[13] J. Rusz, S. Bhowmick, M. Eriksson, N. Karlsson, Scattering of electron vortex beams on a magnetic crystal: Towards atomic-resolution magnetic measurements, Phys. Rev. B 89 (2014) 134428. `doi:10.1103/PhysRevB.89.134428`.
URL `http://link.aps.org/doi/10.1103/PhysRevB.89.134428`

[14] J. Rusz, J.-C. Idrobo, S. Bhowmick, Achieving atomic resolution magnetic dichroism by controlling the phase symmetry of an electron probe, Phys. Rev. Lett. 113 (2014) 145501. `doi:10.1103/PhysRevLett.113.145501`.
URL `http://link.aps.org/doi/10.1103/PhysRevLett.113.145501`

[15] J. C. Idrobo, J. Rusz, J. Spiegelberg, M. A. McGuire, C. T. Symons, R. R. Vatsavai, C. Cantoni, A. R. Lupini, Detecting magnetic ordering with atomic size electron

probes, Advanced Structural and Chemical Imaging 2 (1) (2016) 5. `doi:10.1186/`
`s40679-016-0019-9`.

[16] J. Rusz, S. Bhowmick, Boundaries for efficient use of electron vortex beams to measure magnetic properties, Phys. Rev. Lett. 111 (2013) 105504. `doi:10.1103/`
`PhysRevLett.111.105504`.
URL `http://link.aps.org/doi/10.1103/PhysRevLett.111.105504`

[17] P. Schattschneider, S. Löffler, M. Stöger-Pollach, J. Verbeeck, Is magnetic chiral dichroism feasible with electron vortices?, Ultramicroscopy 136 (2014) 81–85. `arXiv:`
`1304.7976`, `doi:10.1016/j.ultramic.2013.07.012`.

[18] B. Warot-Fonrose, F. Houdellier, M. Hÿtch, L. Calmels, V. Serin, E. Snoeck, Mapping inelastic intensities in diffraction patterns of magnetic samples using the energy spectrum imaging technique, Ultramicroscopy 108 (5) (2008) 393 – 398. `doi:10.1016/j.ultramic.2007.05.013`.

[19] P. Schattschneider, C. Hébert, S. Rubino, M. Stöger-Pollach, J. Rusz, P. Novák, Magnetic circular dichroism in EELS: Towards 10 nm resolution, Ultramicroscopy 108 (5) (2008) 433 – 438. `doi:10.1016/j.ultramic.2007.07.002`.

[20] P. Schattschneider, M. Stöger-Pollach, S. Rubino, M. Sperl, C. Hurm, J. Zweck, J. Rusz, Detection of magnetic circular dichroism on the two-nanometer scale, Phys. Rev. B 78 (10) (2008) 104413. `doi:10.1103/PhysRevB.78.104413`.

[21] J. Salafranca, J. Gazquez, N. Pérez, A. Labarta, S. T. Pantelides, S. J. Pennycook, X. Batlle, M. Varela, Surfactant organic molecules restore magnetism in metal-oxide nanoparticle surfaces, Nano Letters 12 (5) (2012) 2499–2503. `doi:`
`10.1021/nl300665z`.

[22] T. Thersleff, J. Rusz, S. Rubino, B. Hjörvarsson, Y. Ito, N. J. Zaluzec, K. Leifer, Quantitative analysis of magnetic spin and orbital moments from an oxidized iron (1 1 0) surface using electron magnetic circular dichroism, Sci. Rep. 5 (2015) 13012. `doi:10.1038/srep13012`.

[23] D. Song, L. Ma, S. Zhou, J. Zhu, Oxygen deficiency induced deterioration in mi-

crostructure and magnetic properties at y3fe5o12/pt interface, Applied Physics Letters 107 (4) (2015) 042401. `doi:10.1063/1.4927551`.

[24] T. Thersleff, J. Rusz, B. Hjörvarsson, K. Leifer, Detection of magnetic circular dichroism with subnanometer convergent electron beams, Physical Review B 94 (13) (2016) 134430. `doi:10.1103/PhysRevB.94.134430`.

[25] J. Verbeeck, C. Hébert, S. Rubino, P. Novák, J. Rusz, F. Houdellier, C. Gatel, P. Schattschneider, Optimal aperture sizes and positions for EMCD experiments, Ultramicroscopy 108 (9) (2008) 865 – 872. `doi:10.1016/j.ultramic.2008.02.007`.

[26] J. Rusz, J. C. Idrobo, Aberrated electron probes for magnetic spectroscopy with atomic resolution: Theory and practical aspects, Phys. Rev. B 93 (2016) 104420. `doi:10.1103/PhysRevB.93.104420`.
URL `http://link.aps.org/doi/10.1103/PhysRevB.93.104420`

[27] P. Schattschneider, M. Nelhiebel, H. Souchay, B. Jouffrey, The physical significance of the mixed dynamic form factor, Micron 31 (4) (2000) 333 – 345. `doi:10.1016/S0968-4328(99)00112-2`.

[28] S. Löffler, V. Motsch, P. Schattschneider, A pure state decomposition approach of the mixed dynamic form factor for mapping atomic orbitals, Ultramicroscopy 131 (2013) 39 – 45. `arXiv:1210.2947`, `doi:10.1016/j.ultramic.2013.03.021`.
URL `http://www.sciencedirect.com/science/article/pii/S0304399113000910`

[29] S. Löffler, P. Schattschneider, Transition probability functions for applications of inelastic electron scattering, Micron 43 (9) (2012) 971 – 977. `arXiv:1112.5607`, `doi:10.1016/j.micron.2012.03.020`.
URL `http://www.sciencedirect.com/science/article/pii/S0968432812001047`

[30] E. J. Kirkland, Advanced computing in electron microscopy, Plenum Press, 1998.
URL `http://aleph.ub.tuwien.ac.at/F/?func=direct&doc_number=000274136&local_base=TUW01`

[31] C. Hébert, P. Schattschneider, S. Rubino, P. Novak, J. Rusz, M. Stöger-Pollach, Magnetic circular dichroism in electron energy loss spectrometry, Ultramicroscopy 108 (3) (2008) 277 – 284. `doi:10.1016/j.ultramic.2007.07.011`.

[32] J. Rusz, S. Rubino, P. Schattschneider, First-principles theory of chiral dichroism in electron microscopy applied to 3d ferromagnets, Phys. Rev. B 75 (21) (2007) 214425. `doi:10.1103/PhysRevB.75.214425`.

[33] I. Ennen, S. Löffler, C. Kübel, D. Wang, A. Auge, A. Hütten, P. Schattschneider, Site-specific chirality in magnetic transitions, J. Magn. Magn. Mater. 324 (18) (2012) 2723 – 2726. `doi:10.1016/j.jmmm.2012.03.050`.

[34] J. Rusz, O. Eriksson, P. Novák, P. M. Oppeneer, Sum rules for electron energy loss near edge spectra, Phys. Rev. B 76 (6) (2007) 060408. `doi:10.1103/PhysRevB.76.060408`.

[35] H. Lidbaum, J. Rusz, A. Liebig, B. Hjörvarsson, P. M. Oppeneer, E. Coronel, O. Eriksson, K. Leifer, Quantitative magnetic information from reciprocal space maps in transmission electron microscopy, Phys. Rev. Lett. 102 (2009) 037201. `doi:10.1103/PhysRevLett.102.037201`.

[36] Z. Wang, X. Zhong, R. Yu, Z. Cheng, J. Zhu, Quantitative experimental determination of site-specific magnetic structures by transmitted electrons, Nature communications 4 (1) (2013) 1395. `doi:10.1038/ncomms2323`.

[37] J. A. Nelder, R. Mead, A simplex method for function minimization, The Computer Journal 7 (4) (1965) 308–313. `doi:10.1093/comjnl/7.4.308`.

[38] P. Schattschneider, S. Rubino, M. Stöger-Pollach, C. Hébert, J. Rusz, L. Calmels, E. Snoeck, Energy loss magnetic chiral dichroism: A new technique for the study of magnetic properties in the electron microscope (invited), J. Appl. Phys. 103 (7) (2008) 07D931. `doi:10.1063/1.2836680`.

[39] S. Löffler, P. Schattschneider, A software package for the simulation of energy-loss magnetic chiral dichroism, Ultramicroscopy 110 (7) (2010) 831–835. `doi:10.1016/j.ultramic.2010.02.044`.

[40] J. RUSZ, P. OPPENEER, H. LIDBAUM, S. RUBINO, K. LEIFER, Asymmetry of the two-beam geometry in EMCD experiments, Journal of Microscopy 237 (3) (2010) 465–468. `doi:10.1111/j.1365-2818.2009.03295.x`.
URL `http://dx.doi.org/10.1111/j.1365-2818.2009.03295.x`

[41] D. Song, Z. Wang, J. Zhu, Effect of the asymmetry of dynamical electron diffraction on intensity of acquired EMCd signals, Ultramicroscopy 148 (2015) 42–51. `doi:10.1016/j.ultramic.2014.08.012`.

[42] S. Muto, K. Tatsumi, J. Rusz, Parameter-free extraction of {EMCD} from an energy-filtered diffraction datacube using multivariate curve resolution, Ultramicroscopy 125 (0) (2013) 89 – 96. `doi:10.1016/j.ultramic.2012.09.008`.

[43] R. F. Egerton, Electron Energy-Loss Spectroscopy in the Electron Microscope, 2nd Edition, Plenum Press, New York, 1996.

[44] P. Schattschneider, J. Verbeeck, A. Hamon, Real space maps of atomic transitions, Ultramicroscopy 109 (7) (2009) 781 – 787. `doi:10.1016/j.ultramic.2009.01.016`.

[45] J. Verbeeck, P. Schattschneider, S. Lazar, M. Stöger-Pollach, S. Löffler, A. Steiger-Thirsfeld, G. Van Tendeloo, Atomic scale electron vortices for nanoresearch, Appl. Phys. Lett. 99 (20) (2011) 203109. `arXiv:1405.7247`, `doi:10.1063/1.3662012`.
URL `http://link.aip.org/link/?APL/99/203109/1`

[46] H. L. Xin, H. Zheng, On-column 2p bound state with topological charge ±1 excited by an atomic-size vortex beam in an aberration-corrected scanning transmission electron microscope, Microsc. Microanal. 18 (2012) 711–719. `doi:10.1017/S1431927612000499`.

[47] S. Löffler, P. Schattschneider, Elastic propagation of fast electron vortices through crystals, Acta Crystallographica Section A 68 (4) (2012) 443 – 447. `arXiv:1111.6050`, `doi:10.1107/S0108767312013189`.